Optics and Lasers in Engineering 124 (2020) 105843

Contents lists available at ScienceDirect

Optics and Lasers in Engineering

journal homepage: www.elsevier.com/locate/optlaseng

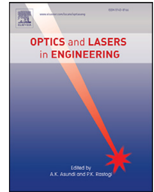

A simplified reflection-mode digital gradient sensing technique for measuring surface slopes, curvatures and topography

Chengyun Miao, Hareesh V. Tippur*

Department of Mechanical Engineering, Auburn University, AL 36849, USA

A R T I C L E I N F O

Keywords:
Optical metrology
Speckle correlation
Surface slopes
Surface topography
Thin films

A B S T R A C T

A simplified optical apparatus for reflection-mode Digital Gradient Sensing methodology (r -DGS) to perform full-field measurement of surface slopes is proposed. It eliminates the need for a beam splitter to record random speckles off a target and via the specular specimen normally. Instead, the target plane speckles reflected off the specimen surface are directly recorded at a known inclination angle. This simplification results in a highly efficient optical arrangement in terms of light loss intrinsic to the original apparatus that used a beam splitter. The simplified apparatus, however, requires altering the governing equations while interpreting the correlated speckle fields in the reference and deformed states. The details of these issues as well as successful demonstrations of *simplified* r-DGS to measure deflection of thin Si wafer subjected to flexure is reported. The modified approach is also demonstrated to study crack-tip deformations near an edge crack in a beam.

1. Introduction

Specular structures are part of many optical and electronic elements and devices; e.g., lenses, silicon wafers, mirrors, photovoltaics, etc. The constituent materials in these are generally stiff, brittle and often thin and their surface profile plays a critical role in their performance. Also, they undergo deformations and potentially fail due to thermo-mechanical stresses during service. In this context, precise measurement of surface profile changes and the resulting stresses in these materials and devices over large fields-of-view with ultrahigh sensitivities is indeed valuable.

There are many non-contact and full-field slope measurement optical techniques capable of quantifying full-filed evaluation of surface slopes of thin structures. Advantage of such methods is that (a) surface topography can be obtained by numerically integrating the measured surface slopes, (b) the curvatures and hence stresses can be estimated by just a single differentiation of measured surface slope data. These methods can be divided into two broad categories, incoherent and coherent illumination methods. Lichtenberg [1] proposed an incoherent illumination method based on reflection moiré to determine slopes of specular objects. Rieder and Ritter [2] modified Lichtenberg's experimental setup by introducing a half-mirror so that a dark spot disrupting the moiré pattern in the original setup is eliminated. Kao and Chiang [3] reported a family of grating based moiré techniques for slope and curvature measurements. The coherent illumination methods are generally interferometric in nature. Chiang and Juang [4] proposed laser speckle interferometry to study slope contours of bent plates made of almost any material. Assa et al. [5] developed several grating shearing interferometers to record slopes and curvatures of flexed plates. Tippur et al. [6,7] proposed a double-grating interferometry called Coherent Gradient Sensing (CGS), which can be used to quantify surface slopes and curvatures of thin structures based on the angular deflections of light rays. Udupa et al. [8] investigated subsurface defects in an unpolished silicon wafer using digital shearography. Although the moiré and interferometric techniques have been popular over the years, disadvantages such as the need for physical gratings, coherent light source, conversion of analog optical fringes into digital information, to name a few, are all obvious.

Recently, a full-field optical method called Digital Gradient Sensing (DGS) based on 2D Digital Image Correlation has been introduced for measuring two orthogonal angular deflections of light rays [9,10]. The two variants of DGS, a transmission-mode DGS (t-DGS) for measuring stress gradients in transparent solids, and a reflection-mode DGS (r-DGS) for measuring surface slopes on optically reflective objects are shown not only feasible but very attractive for experimental mechanics investigations due to simplicity of the optical setup and its measurement accuracy besides multitude of advantages such as full-field digital measurements, availability of results as data arrays in the region-of-interest (ROI), ubiquity of computational power, continued progress in terms of efficient and accurate image correlation algorithms, to name a few. Zhang et al. [11] applied t-DGS along with a numerical model to study contact stress concentration problem involving line-load acting on the

* Corresponding author.
E-mail address: tippuhv@auburn.edu (H.V. Tippur).

https://doi.org/10.1016/j.optlaseng.2019.105843
Received 10 July 2019; Received in revised form 17 August 2019; Accepted 27 August 2019
0143-8166/© 2019 Elsevier Ltd. All rights reserved.

edge of a large planar sheet. Hao et al. [12] explored fiber pull-out problem using *t*-DGS. Zhang et al. [13] investigated surface topography and thin film stresses in film/substrate systems at elevated temperatures using *r*-DGS. Jain and Tippur [14] explored static and dynamic fracture mechanics of polymer beams using *r*-DGS. Later on, the same authors [15] extended *r*-DGS to study transient out-of-plane deformations and damage in planar isotropic and orthotropic plates. By coupling *r*-DGS with an efficient 2D least-squares integration scheme called Higher-order Finite-difference-based Least-squares Integration or HFLI, surface topography of thin structures with sub-micron resolution over large ROI has been achieved [16,17]. Subsequently, Miao and Tippur [18] have examined the measurement accuracy of such measurements from *r*-DGS used in conjunction with HFLI. They have found that the accuracy is influenced by the temporal frequency of the recording device. Ultrahigh-speed digital photography at 10^6 frames per second resulted in nanoscale (10–20 nm) out-of-plane deformation measurement accuracy over relatively large (75×75 mm^2) ROI whereas slower recording speeds of 10^1 frames per second decreased the accuracy to sub-micron levels (300–400 nm). By combining *r*-DGS with *t*-DGS, the authors have also proposed two variants of DGS of higher measurement sensitivity suitable for studying high-stiffness and ultralow-toughness transparent solids such as soda-lime glass [19]. Although *r*-DGS and its variants have been developed and demonstrated as powerful optical tools, their experimental setups and implementation could be a bit complicated for the beginner when compared to the *t*-DGS counterpart as they all require a beam splitter placed at 45° relative to the specimen and speckle target pair. This requires precise alignment of the beam splitter relative to the target and the specimen for its successful implementation. Furthermore, the physical size of the beam splitter relative to the ROI to be studied is also important and could be a hindrance when large ROI are to be interrogated. Equally important is that a substantial amount of light (~75% of the light emanating from the speckle target) is wasted due to the beam splitter. Therefore, eliminating the beam splitter from the setup to simplify the *r*-DGS approach is significant in terms of practical implementation. It also has implications on the governing equations and the associated data analysis as demonstrated in the current research.

In the following, the principles of *r*-DGS are briefly reviewed. Next, the experimental setup and governing equations of the *simplified r*-DGS without the beam splitter are described. Then, this new variant of DGS is verified by measuring surface slopes and curvatures of a Si wafer subjected to central out-of-plane loading. Subsequently, the feasibility of *simplified r*-DGS methodology to study more complex fracture mechanics problems is demonstrated. Finally, the major results of this research are summarized.

2. Traditional reflection-mode digital gradient sensing (*r*-DGS)

2.1. Experimental setup and working principle

A schematic of the experimental setup for traditional reflection-mode Digital Gradient Sensing (*r*-DGS) to measure surface slopes is shown in Fig. 1. A digital camera is used to record random speckles on a target plane via the reflective specimen surface. To achieve this, the specimen and the target plates are placed perpendicular to each other, and the beam splitter is positioned at 45° relative to the specimen and target plate pair. The target plate is spray painted with random black and white spray speckles, and illuminated uniformly using a broad spectrum (white) light. The specimen surface is made reflective by depositing aluminum film if it is not specular. When the specimen is in the undeformed state, the gray scale at a generic point P on the target plate is photographed by a camera pixel through point O on the specimen plane. Thus recorded speckle image at that time instant and/or load level is the reference image. After the specimen suffers deformation due to the applied load, the gray scale at a neighboring point of P, namely Q on the target plate, is photographed by the same pixel through the same point O on the specimen surface. The corresponding image of the specimen in the deformed state is recorded next as an assemblage of all individual pixel gray scales. The *local* orthogonal speckle displacements at each pixel are identified as $\{\delta_x, \delta_y\}$ in Fig. 2 and can be obtained by performing a 2D correlation of the reference and deformed images. The corresponding angles $\{\phi_x, \phi_y\}$ representing two orthogonal angular deflections of light rays can then be obtained as shown in Fig. 2.

For simplicity, only the angular deflections of light rays in the *y*-*z* plane are shown in Fig. 2 and similar arguments are valid in the *x*-*z* plane as well. Here, $\underline{OQ}$ makes an angle ϕ_y with $\underline{OP}$. Further, $\phi_y = \theta_i + \theta_r$ where θ_i and $\theta_r(=\theta_i)$ are incident and reflected angles relative to the normal to the specimen and $\underline{n}$ denotes the local normal to the deformed surface. A similar relationship in the *x*-*z* plane can be obtained as well. Then, the two orthogonal surface slopes of the surface can be related to $\{\phi_x, \phi_y\}$, as $\{\frac{\partial w}{\partial x} = \frac{1}{2}\tan(\phi_x), \frac{\partial w}{\partial y} = \frac{1}{2}\tan(\phi_y)\}$. The governing equations

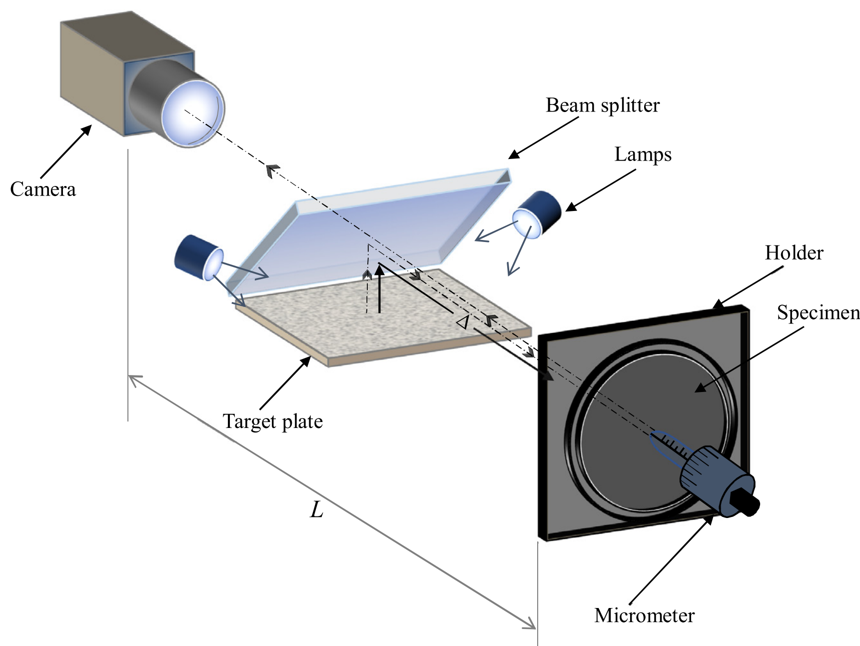

Fig. 1. Schematic of traditional *r*-DGS experimental setup [16].

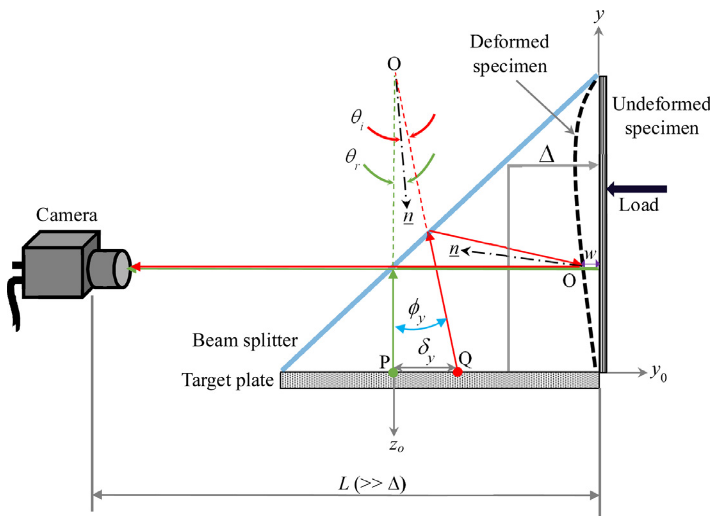

Fig. 2. Working principle of traditional *r*-DGS [18].

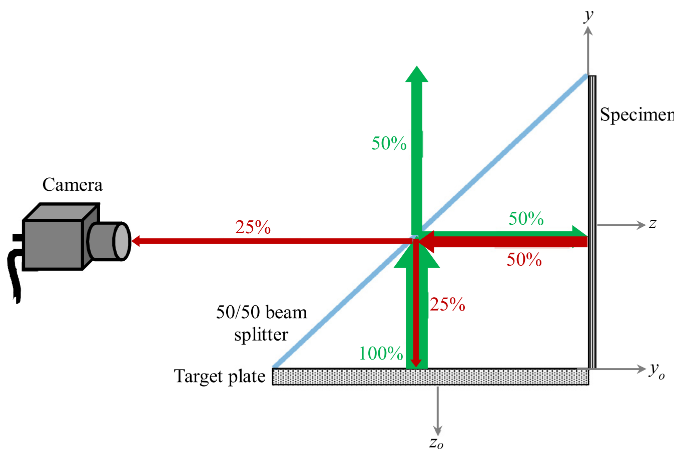

Fig. 3. Light ray diagram of traditional *r*-DGS depicting loss of light in the apparatus due to the beam splitter.

for *r*-DGS thus are [10],

$$\frac{\partial w}{\partial x} = \frac{1}{2}\tan\left(\phi_x\right) \approx \frac{1}{2}\left(\phi_x\right) \approx \frac{1}{2}\left(\frac{\delta_x}{\Delta}\right)$$
$$\frac{\partial w}{\partial y} = \frac{1}{2}\tan\left(\phi_y\right) \approx \frac{1}{2}\left(\phi_y\right) \approx \frac{1}{2}\left(\frac{\delta_y}{\Delta}\right) \tag{1}$$

where Δ is the distance or the gap between the specimen and target planes, and small angle approx. is invoked. It is important to note that the coordinates of the specimen plane are utilized for describing the governing equations and the camera is focused on the target plane during photography. Therefore, mapping of coordinates is needed to transfer the target plane locations to the specimen plane. This can be done using the pin-hole camera approximation, $\{x = \frac{L}{L+\Delta} \times x_0,\ y = \frac{L}{L+\Delta} \times y_0\}$, where $\{x, y\}$ and $\{x_0, y_0\}$ represent the coordinates of the specimen and target planes, respectively, and L is the distance between the specimen and the camera [18].

2.2. Disadvantages of traditional setup of r-DGS

A significant amount of light emanating from the speckle target is wasted due to the presence of the 50/50 beam splitter (see, Fig. 3) in the apparatus. That is, when a light wave that originates from the target plate reaches the beam splitter, half of the light ray passes through the beam splitter, and the other half is reflected towards to the specimen. Then, the light wave is reflected back towards to the beam splitter and again, only one half of that passes through the beam splitter to be captured by the camera. Thus, under ideal conditions only 25% of the light emanating from the speckle target is captured by the camera. In reality, however, the light ray captured by camera is lower due to other losses. Such a huge loss of light may not be a problem for recording low-speed events. However, it introduces difficulties to ultrahigh-speed photography at 10^6 frames per second or higher, typical of stress wave induced events. Moreover, the beam splitter adds to the complexity of the *r*-DGS experimental setup in terms of positioning it precisely at 45°. The physical size of it also needs to be large if large ROI are to be studied (e.g., metrology of large diameter Si wafers). Considering the core principle of *r*-DGS that the camera needs to be focused on the target via the reflective specimen surface to record speckles, and the beam splitter is an auxiliary optical element relative to the *t*-DGS setup, possibility of a simpler variant of *r*-DGS method without using the beam splitter is very attractive. Furthermore, the simplicity of the setup could have an impact on measurement precision as the number of optical elements in the apparatus is reduced, thus avoiding additional optical aberrations and alignment issues.

3. *Simplified r*-DGS setup

The sideview of the experimental setup for *r*-DGS without the beam splitter is shown in Fig. 4(a). Let (y, z) and (y_o, z_o) be the in-plane coordinates of the specimen and target planes, respectively. The schematic here is similar to the setup for traditional *r*-DGS, except the specimen is rotated about the x-axis relative to the target plate by $\alpha = 45°$ (The choice of the angle is based on convenience and other more suitable angles can be used as well.) The light rays originating from the target plate get reflected by the specular specimen surface towards to the camera. Thus, the speckles on the target are recorded by the camera via the specimen surface directly. Unlike the traditional *r*-DGS, in this simplified setup, the gap between the specimen plane and the target, also defined as Δ, is continuously (linearly) changing from Δ_M to Δ_N, as shown in Fig. 4(a). The appropriate local measurement of Δ will be explained later on in the experimental section. As in *r*-DGS, the distance from the center of specimen to the camera is defined as L. (It should be noted here that light rays are shown to be parallel to the optical axis in Fig. 4(a), while the incident light from the points located away from the specimen center is ideally inclined. However, since the camera is placed sufficiently far away from the target and the angle-of-view of the imaging system is less than 1.8°, it is reasonable to represent the light rays paraxially.

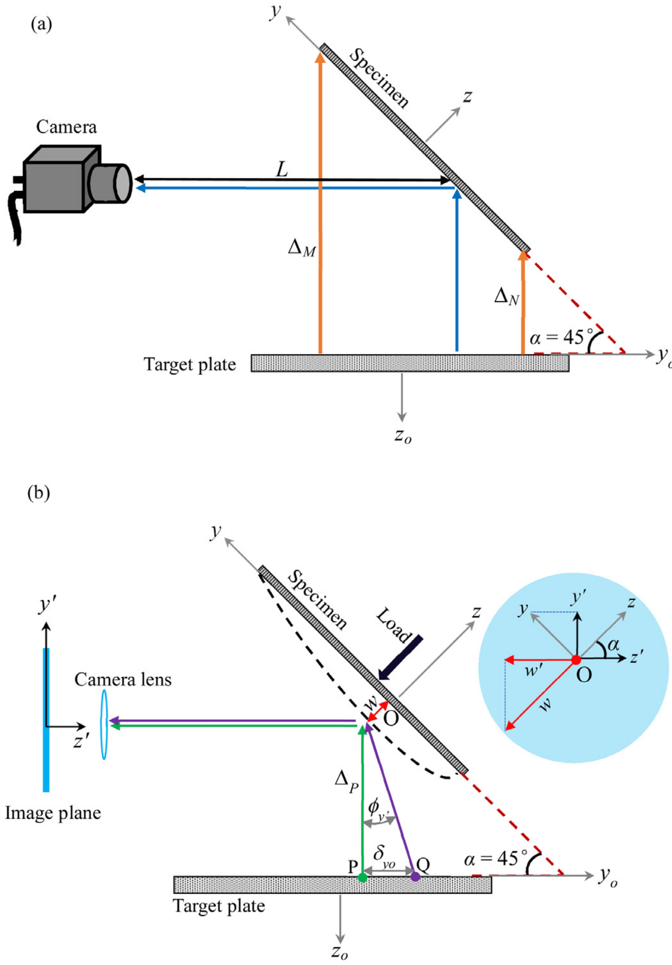

Fig. 4. Simplified *r*-DGS without beam splitter: (a) schematic, (b) working principle (Inset in the shaded circle shows relation between specimen and global coordinate systems).

Furthermore, using a telecentric lens is an alternative option [20–22] in this regard.)

The angular deflections of light rays are shown in Fig. 4(b). When the specimen is in the undeformed state, the gray scale at a generic point P on the target plate is photographed by a camera pixel through point O on the specimen plane. Thus, the recorded image at that time instant and/or load level is the reference image. After the specimen suffers deformation, say, due to an applied load (the load need not be along the *z*-direction), the gray scale at a neighboring point of P, namely Q on the target plate is photographed by the same pixel through the same point O on the specimen surface. The corresponding image of the specimen in the deformed state is recorded next as an assembly of all such individual pixel gray scales. The local orthogonal speckle displacements $\{\delta_{yo}, \delta_{xo}\}$ can be obtained by performing a 2D image correlation of the reference and deformed images. The corresponding angles $\{\phi_{y'}, \phi_{x'}\}$ represent two orthogonal angular deflections of light rays where primes denote global coordinates of the setup as shown in the Fig. 4(b) inset. It should be noted that, the out-of-plane deformation (w) is along the *z*-axis of the specimen coordinates (x, y, z). However, the images recorded by the camera are in the (x', y', z') coordinates. The details of these two coordinate systems are shown in the inset of Fig. 4(b). From the figure it can be observed that,

$$\frac{w'}{w} = \frac{y'}{y} = \cos\alpha(=45^\circ) = \frac{1}{\sqrt{2}} \qquad x' = x \tag{2}$$

Hence, $\{\phi_{y'}, \phi_{x'}\}$ is related to $\{\frac{\partial w'}{\partial y'}, \frac{\partial w'}{\partial x'}\}$ as,

$$\begin{aligned}\frac{\partial w'}{\partial y'} &= \frac{1}{2}\tan(\phi_{y'}) \approx \frac{1}{2}(\phi_{y'}) \approx \frac{1}{2}\left(\frac{\delta_{yo}}{\Delta_P}\right)\\ \frac{\partial w'}{\partial x'} &= \frac{1}{2}\tan(\phi_{x'}) \approx \frac{1}{2}(\phi_{x'}) \approx \frac{1}{2}\left(\frac{\delta_{xo}}{\Delta_P}\right)\end{aligned} \tag{3}$$

where Δ_P is the local gap (distance) between the specimen and target planes at point *P*. The Eq. (3) is silimar to Eq. (1), which is the governing equation for traditional *r*-DGS. Next, $\{\frac{\partial w'}{\partial y'}, \frac{\partial w'}{\partial x'}\}$ needs to be transformed to obtain the specimen surface slopes, $\{\frac{\partial w}{\partial y}, \frac{\partial w}{\partial x}\}$, using the equations above as:

$$\begin{aligned}\frac{\partial w}{\partial y} &= \frac{\partial\left(\sqrt{2}w'\right)}{\partial\left(\sqrt{2}y'\right)} = \frac{\partial w'}{\partial y'} \approx \frac{1}{2}\left(\frac{\delta_{yo}}{\Delta_P}\right);\\ \frac{\partial w}{\partial x} &= \frac{\partial\sqrt{2}w'}{\partial x'} = \sqrt{2}\frac{\partial w'}{\partial x'} \approx \frac{\sqrt{2}}{2}\left(\frac{\delta_{xo}}{\Delta_P}\right) = \frac{1}{\sqrt{2}}\left(\frac{\delta_{xo}}{\Delta_P}\right)\end{aligned} \tag{4}$$

It should be noted that the experimental setup shown here has the specimen rotated about the *x*-axis, which had led to $x = x'$, $y = \sqrt{2}y'$, but $\frac{\partial w}{\partial y} = \frac{\partial w'}{\partial y'}$, $\frac{\partial w}{\partial x} = \sqrt{2}\frac{\partial w'}{\partial x'}$. (Also, it can be concluded that when the experimental setup is rotated about the *y*-axis instead, the governing equations will be $x = \sqrt{2}x'$, $y = y'$, and $\frac{\partial w}{\partial y} = \sqrt{2}\frac{\partial w'}{\partial y'}$, $\frac{\partial w}{\partial x} = \frac{\partial w'}{\partial x'}$.) As noted earlier, in this *simplified r*-DGS method, the angle α, between the specimen and target planes is selected to be 45°. If any other convenient angle is more suitable ($0^\circ < \alpha < 90^\circ$), is theoretically acceptable although 45° is relatively straightforward and often more suitable.

It is important to note that the coordinates of the specimen plane are utilized for describing the governing equations and the camera is focused on the target plane during photography. Therefore, a coordinate mapping is needed to transfer the target plane locations to the specimen plane. This can be done again using the pin-hole camera approximation as, $\{x = \frac{L}{L+(\frac{\Delta_M+\Delta_N}{2})} \times x_o,\ y = \frac{L}{L+(\frac{\Delta_M+\Delta_N}{2})} \times y_o\}$, where $\{x, y\}$ and $\{x_o, y_o\}$ represent the coordinates of the specimen and target planes, respectively [18].

4. Demonstration: silicon wafer subjected to central loading

The feasibility of this new method to measure surface slopes of a deformed thin circular silicon wafer subjected to concentrated central loading is demonstrated next. A schematic of experimental setup and a close-up photograph are shown in Fig. 5(a). The specimen used here is similar to the one used in Ref. [16], a single-face polished 360 µm thick 111 type silicon wafer of diameter 50.8 mm. The unpolished face was glued to a thick steel washer with a circular aperture of 30 mm using epoxy. Another steel plate fitted with a micrometer (least-count = 10 μm) at its center was positioned directly behind the silicon wafer. These two steel plates were secured in a holder. A target plate, decorated with random black and white speckles, was placed horizontally at 45° to the silicon wafer (the specimen). A Nikon D100 digital SLR camera was focused on the target via the polished face of the silicon wafer. The camera was fitted with a 70–300 mm lens and an adjustable bellows. A small aperture ($F^{\#} = 22$) was selected to record the speckles with a good depth-of-focus. The distance between the center of the silicon wafer and lens (L) along the optical axis of the setup was ~1448 mm (note that L at other generic locations would be different) whereas the value of $L + \Delta$ is nominally constant at any location ($L + (\frac{\Delta_M+\Delta_N}{2})$) is ~1506 mm in this experiment). An 8-bit reference image was recorded with a resolution of 1504 × 1000 pixels before the silicon wafer was subjected to central deflection. Subsequently, three different out-of-plane displacements, w = 10, 20, 30 μm, were imposed manually using the micrometer during the experiment. The corresponding speckle images in the deformed state were recorded. The close-up view of the experimental setup in Fig. 5(b) and (c) show the simplicity of this new approach.

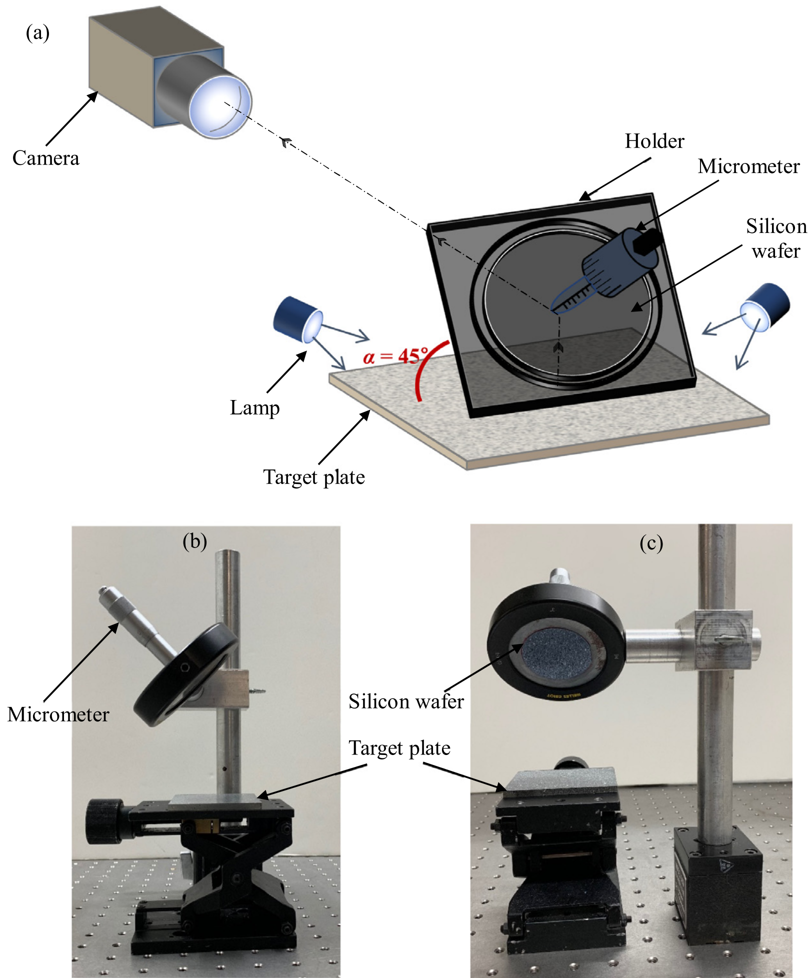

Fig. 5. Schematic of the experimental setup for silicon wafer subjected to central loading (a). Images of side view (b) and front view (c) for the setup. (The target plane speckles are visible in bottom-right photograph because the Si wafer surface is reflective.).

The speckle images in the reference and deformed states of the silicon wafer subjected to central out-of-plane deformation of 10 μm are shown in Fig. 6(a) and (b), respectively. In the experiment, the silicon wafer is circular with a dimeter of 50.8 mm. As the coordinate system of image plane is different from that of the wafer plane, it can be observed that the recorded speckle images here are elliptical in shape, and are contracted in the y' direction. Before performing the experiment, two marks, A and B, were placed on the speckle target to be along the y' (or y_o) direction. The distance AB was selected as 10 mm; the scale factor (SF) of the speckle images was determined as 33.56 µm/pixel in this experiment. The dashed line connecting A and B was extended to the top edge of the image at point M, and the bottom edge of image at point N. Distances of $\underline{MA}$ and $\underline{AN}$ can be calculated based on the scale factor used. During the experiment, Δ_A, shown in Fig. 6(c), was measured as 68 mm, then the Δ_M $(= \Delta_A + MA)$ and Δ_N $(= \Delta_A - AN)$ can be calculated based on the distance $\underline{MA}$ and $\underline{AN}$, and $\alpha = 45°$ Hence, Δ at any location along the y' direction can be calculated. It should be noted that Δ is constant along the x' direction since this experimental setup is tilted about the x'-axis.

All the deformed images were correlated (using ARAMIS image analysis software) with the same reference image to measure the local speckle displacements/shifts $\{\delta_{yo}, \delta_{xo}\}$ in the region-of-interest (ROI). During correlation, a sub-image size of 20 × 20 pixels with 10 pixels overlap was used, and it resulted in 97 × 148 array of slope data points in the field. The local displacements were used to calculate $\{\frac{\partial w}{\partial y}, \frac{\partial w}{\partial x}\}$ based on Eq. (4). Thus obtained surface slope contours, $\{\frac{\partial w}{\partial y}, \frac{\partial w}{\partial x}\}$, are shown in Fig. 7, for different out-of-plane deformations imposed. It can be observed that contours are antisymmetric relative to the horizontal

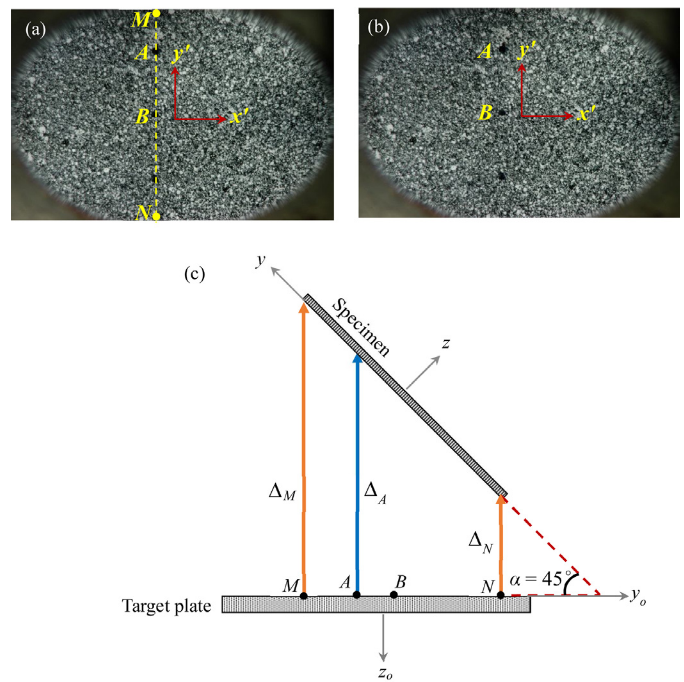

Fig. 6. Speckle images in the reference (a) and deformed (b) states of the silicon wafer subjected to central out-of-plane deformation of 10 µm; (c) illustration for the measurement of Δ.

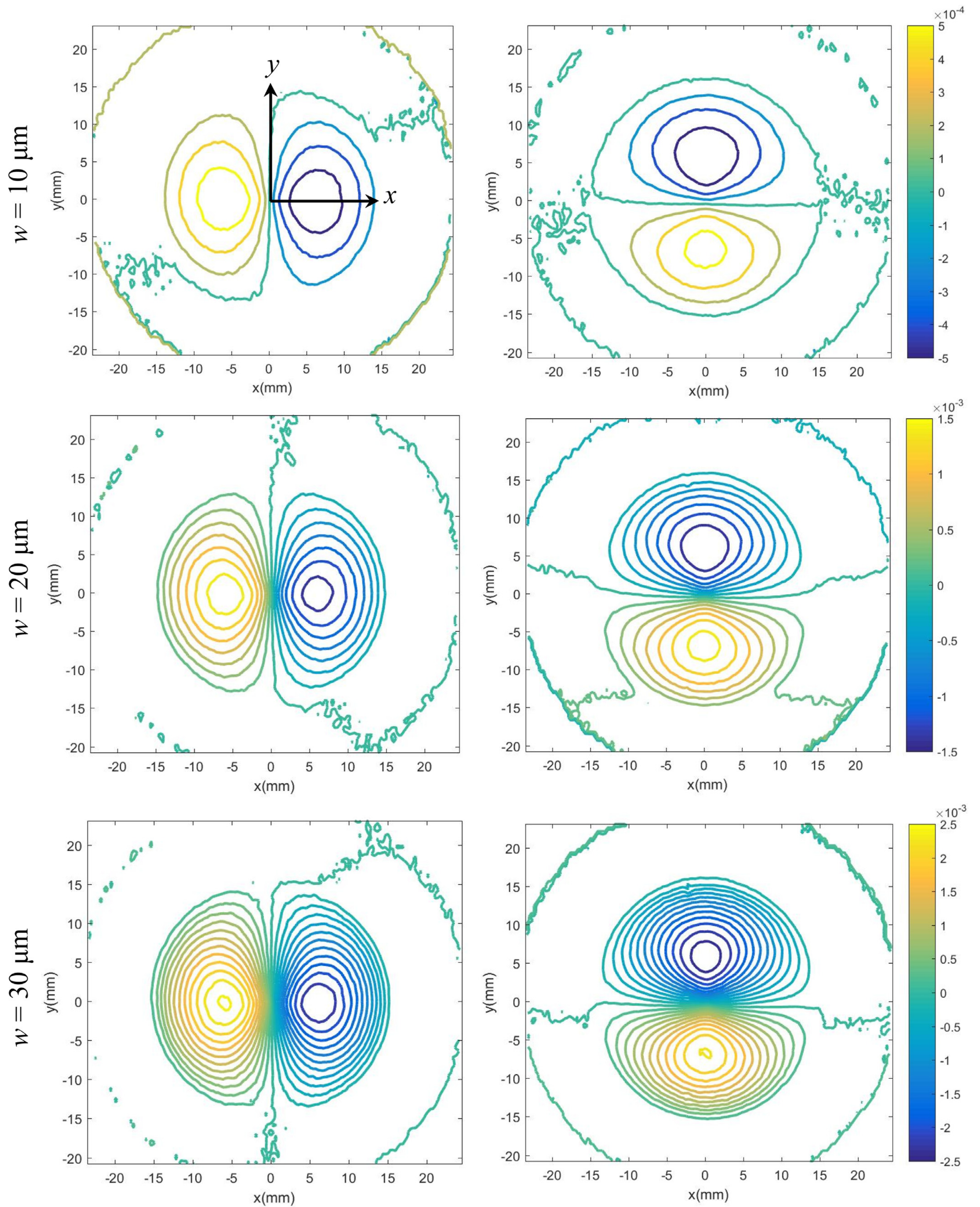

Fig. 7. Surface slopes $w_{,x}$ (left column) and $w_{,y}$ (right column) for a clamped silicon wafer subjected to out-of-plane deformations. Note: (0, 0) is made to coincide with the center of silicon wafer. Contour increments = 2×10^{-4} rad.

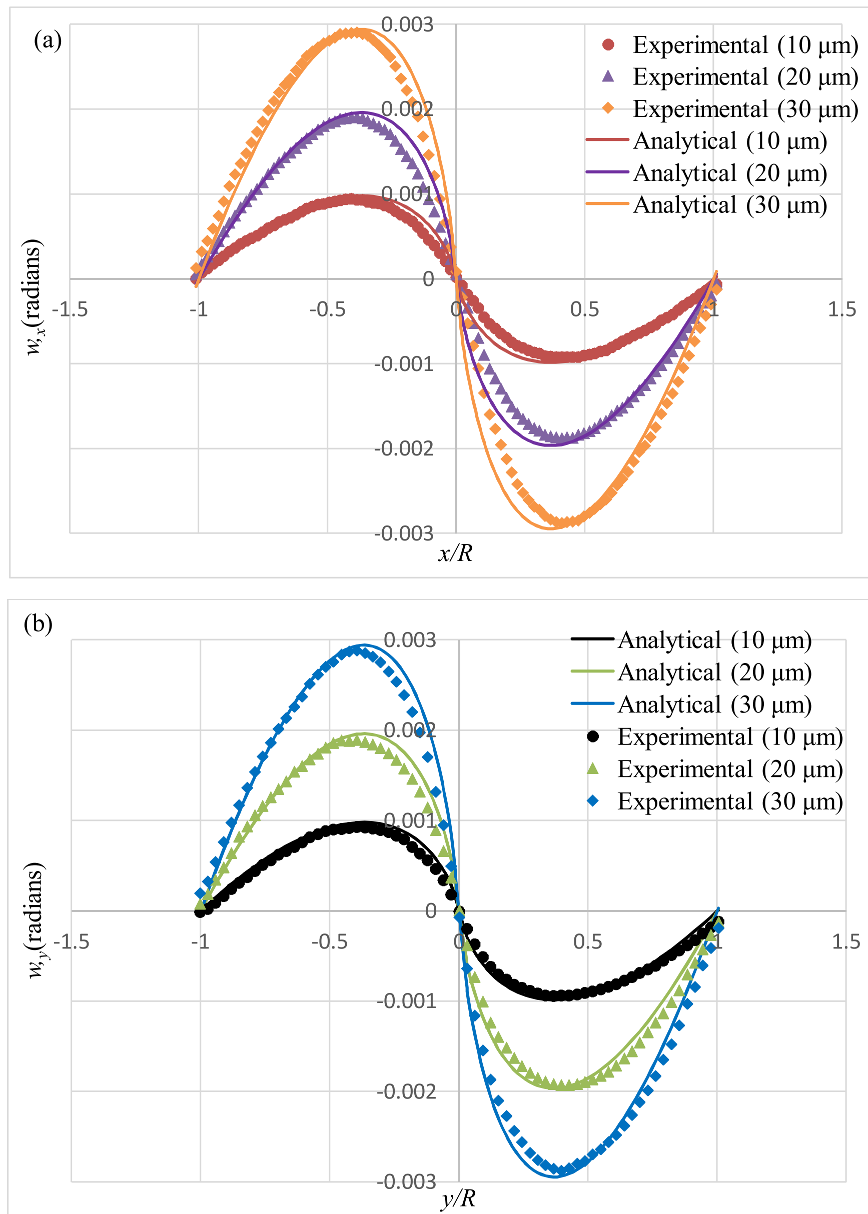

Fig. 8. Comparison of analytical data and experimental data of $w_{,x}$ along the x-axis (a), and $w_{,y}$ along the y-axis (b) corresponding to three different imposed out-of-plane deformations.

or vertical axes in terms of the magnitude with a high concentration in the vicinity of the loading point. Furthermore, both are symmetric relative to the vertical and horizontal axes with the origin coinciding with the loading point. As expected, the contours get denser with larger imposed deflection. There are no contours in the portion of the Si wafer glued to the steel washer as the Si wafer in that region is essentially 'clamped.'

To verify the accuracy of measurements from this new method, the slope contours are compared directly with the analytical solutions for an elastic thin circular plate with a clamped boundary condition subjected to a centrally applied deflection using [16],

$$\frac{\partial w}{\partial x} = \frac{4xw}{R^2}\log\left(\frac{\sqrt{x^2+y^2}}{R}\right)$$
$$\frac{\partial w}{\partial y} = \frac{4yw}{R^2}\log\left(\frac{\sqrt{x^2+y^2}}{R}\right) \tag{5}$$

where w is the out-of-plane deformation and R is the radius of the circular plate. The comparisons made between the experimental and analytical data sets along the x- and y-axes for all three out-of-plane deformations are shown in Fig. 8. It can be observed that there is a very good agreement between the experimental and analytical data in all load cases.

It is shown in Ref. [16] that the two orthogonal surface slopes obtained from traditional r-DGS can be numerically integrated to reconstruct the surface topography using Higher-order Finite-difference-based Least-squares Integration or the HFLI method. Accordingly, the two orthogonal surface slopes obtained from this *simplified* r-DGS method are integrated using HFLI scheme. The reconstructed surface topography and the corresponding contours of out-of-plane displacements (w) are shown in Fig. 9. The peak values of the height of the reconstructed topography are 9.4, 19.6 and 28.7 µm with errors ranging from 2 to 6%. (The errors are attributed to a combined effect of (a) micrometer backlash, (b) optical and electronic noise, (c) errors due to speckle correlation, and (d) integration errors in the HFLI method and hence cannot be readily delineated.) Considering these, the measurement accuracy is very good. The circular contours in the right column of Fig. 9 show that the shape of the reconstructed figures match well with the reality of the experiment both qualitatively and quantitatively. The results here are similar to the results in Ref. [16], and demonstrate

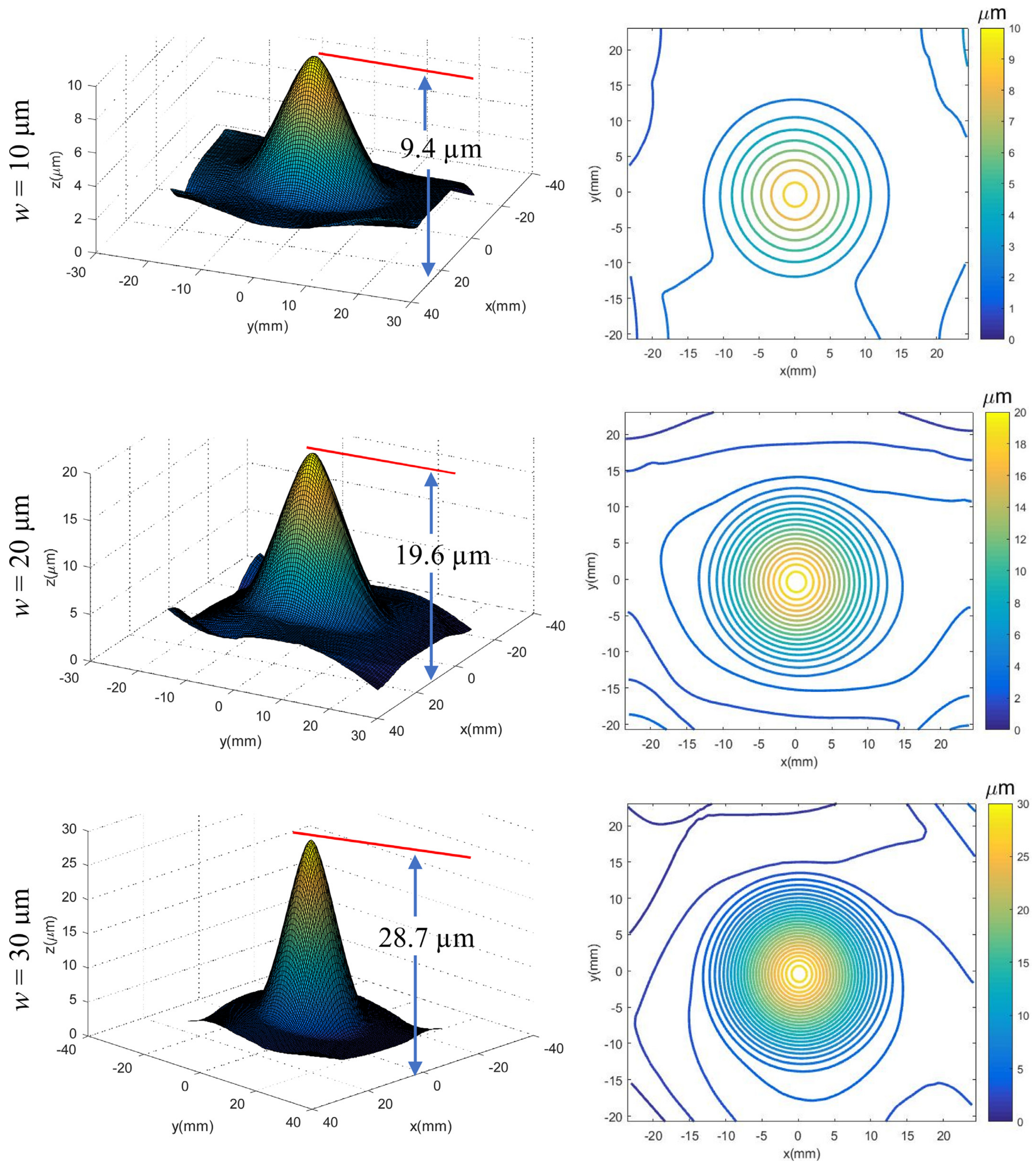

Fig. 9. Surface topography obtained from integrating surface slopes using HFLI method for a clamped silicon wafer subjected to out-of-plane deformations. Left column: 3D surface; Right column: out-of-plane displacement (w) contours (1 μm increment).

that it is feasible to apply this new simplified method with HFLI to reconstruct the surface topography of the deformed Si wafer.

In the semiconductor industry, curvatures of Si wafer are also critical, since stresses can be directly estimated from different curvature components and plate theories. To test that possibility, the curvatures were obtained by differentiating the slopes with respect to the local coordinates and are plotted in Fig. 10. It can be observed that the curvature contours of $\{\frac{\partial^2 w}{\partial x^2}, \frac{\partial^2 w}{\partial y^2}\}$ rapidly increase in the vicinity of the loading point (in the direction of differentiation). Unlike integration, numerical differentiation exaggerates noise in the experimental data. Hence, the curvature contours in Fig. 10 are relatively noisy when compared to the contours in Figs. 7 and 9. For comparison purposes, the curva-

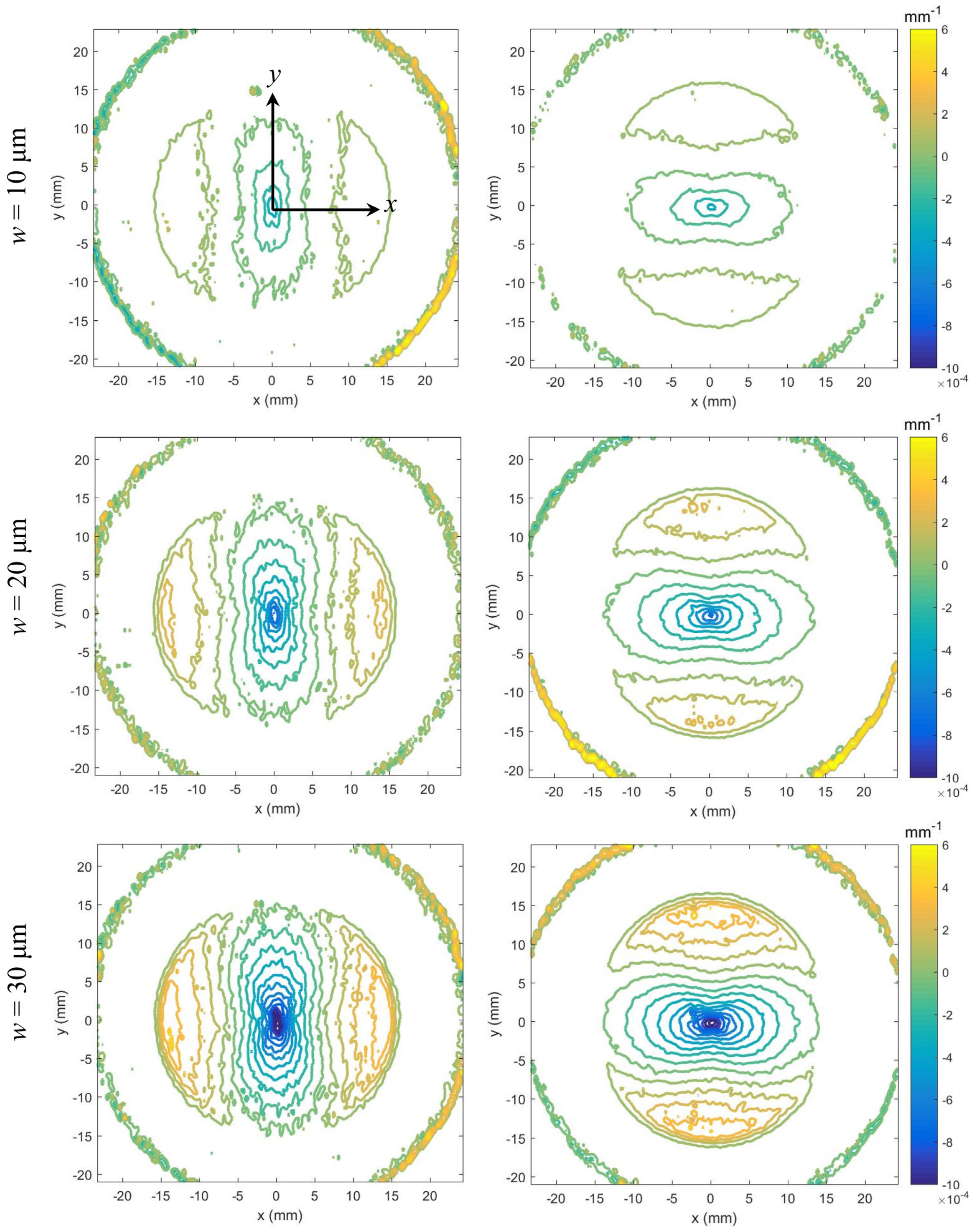

Fig. 10. Curvatures $w,_{xx}$ (left column) and $w,_{yy}$ (right column) for a clamped silicon wafer subjected to out-of-plane deformations. Note: (0, 0) is made to coincide with the center of silicon wafer. Contour increments = 9.3×10^{-5} mm^{-1}.

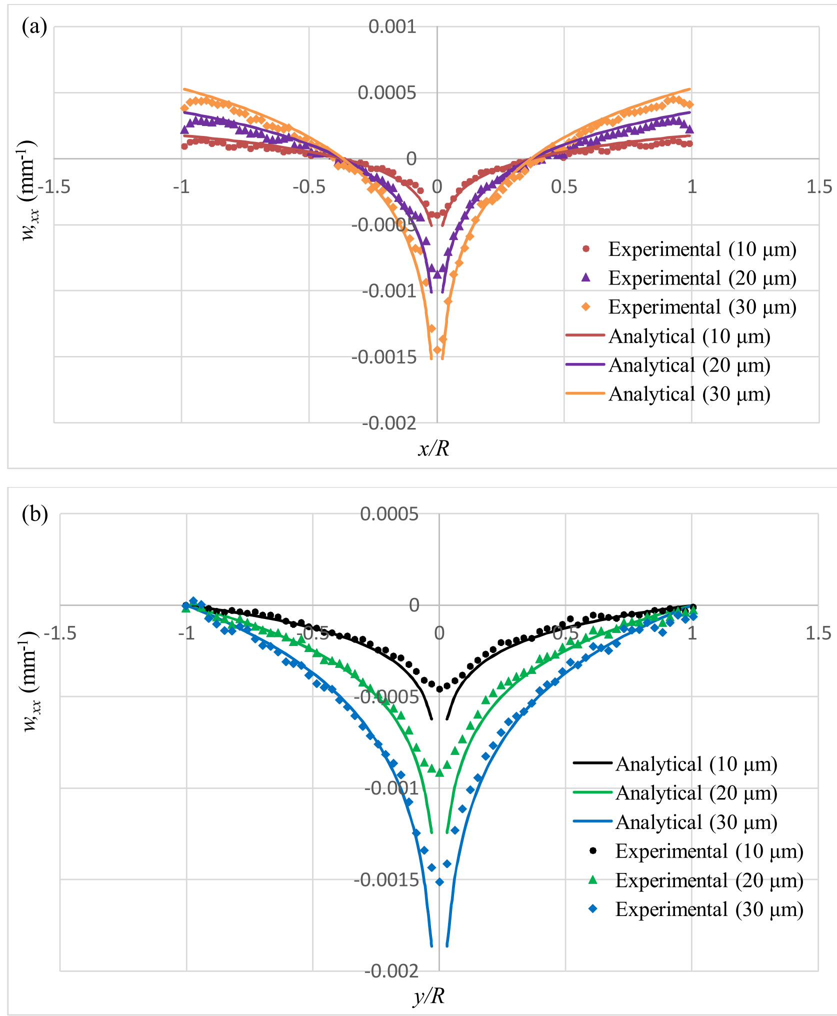

Fig. 11. Comparison of analytical data and experimental data of $w_{,xx}$ along the x-axis (a), and along the y-axis (b) corresponding to three different imposed out-of-plane deformations.

ture contours are compared directly with the analytical solutions given by [7]:

$$\begin{aligned}\frac{\partial^2 w}{\partial x^2} &= \frac{4w}{R^2}\log\left(\frac{\sqrt{x^2+y^2}}{R}\right) + \frac{4x^2 w}{R^2(x^2+y^2)}\\ \frac{\partial^2 w}{\partial y^2} &= \frac{4w}{R^2}\log\left(\frac{\sqrt{x^2+y^2}}{R}\right) + \frac{4y^2 w}{R^2(x^2+y^2)}\end{aligned} \tag{6}$$

The curvatures of $\frac{\partial^2 w}{\partial x^2}$ were selected to make the comparison between experimental and analytical data sets along the x- and y-axes for all three levels of out-of-plane deflection, as shown in Fig. 11. It can be clearly observed that there is a good agreement between the experimental and analytical results in each case. Some deviations can be observed close to the center and edge of the Si wafer where the surface slopes are approaching zero, and where numerical differentiation has introduced larger errors.

For completeness, curvature components $\frac{\partial^2 w}{\partial xy}$ and $\frac{\partial^2 w}{\partial yx}$, also called twist, obtained by differentiating $\frac{\partial w}{\partial x}$ and $\frac{\partial w}{\partial y}$ with respect to the y- and x-variables, respectively, are also plotted in Fig. 12. It can be observed that all the fields are skewed along ±45° directions with dual, equidistant positive and negative contours away from the origin. It is evident that the twist fields of $\frac{\partial^2 w}{\partial xy}$ are nearly identical with those of $\frac{\partial^2 w}{\partial yx}$ both qualitatively and quantitatively further supporting the numerical processing of measured data.

5. Potential to fracture mechanics

The traditional *r*-DGS has been applied to study fracture mechanics problems [14,23] previously. It is therefore important to demonstrate the feasibility of the proposed *simplified r*-DGS methodology to study a fracture mechanics problem that deals with a discontinuity. A PMMA beam with an edge notch and subjected to a symmetric three-point bending was studied. The schematic of the experimental setup along with a photograph is shown in Fig. 13.

A 152 mm × 51 mm × 8.6 mm PMMA specimen, with an initial crack of length 13 mm was used in this demonstration. One of the 152 mm × 51 mm faces was made reflective by depositing it with a thin layer of aluminum. The single edge notched (SEN) specimen was supported on two anvils (span 127 mm), and loaded using an Instron 4465 universal testing machine operating in displacement controlled mode (crosshead speed = 0.004 mm/s). A Nikon D100 digital SLR camera was focused on the target via the reflective surface of PMMA. The camera was fitted with a 70–300 mm lens and an adjustable bellows. A small aperture ($F^{\#} = 22$) was selected to record the speckles with a good depth-of-focus. The distance between the center of PMMA specimen and the end of lens (L) was ∼1320 mm. The largest and smallest distances, Δ_M and Δ_N, were 75 mm and 24 mm, respectively.

An 8-bit reference image was recorded with a sensor resolution of 1504 × 1000 pixels before loading ($F = 0$ N). The speckle images were recorded at every 50 N increments up to a maximum load of 500 N. The images in the deformed state were correlated with the reference image

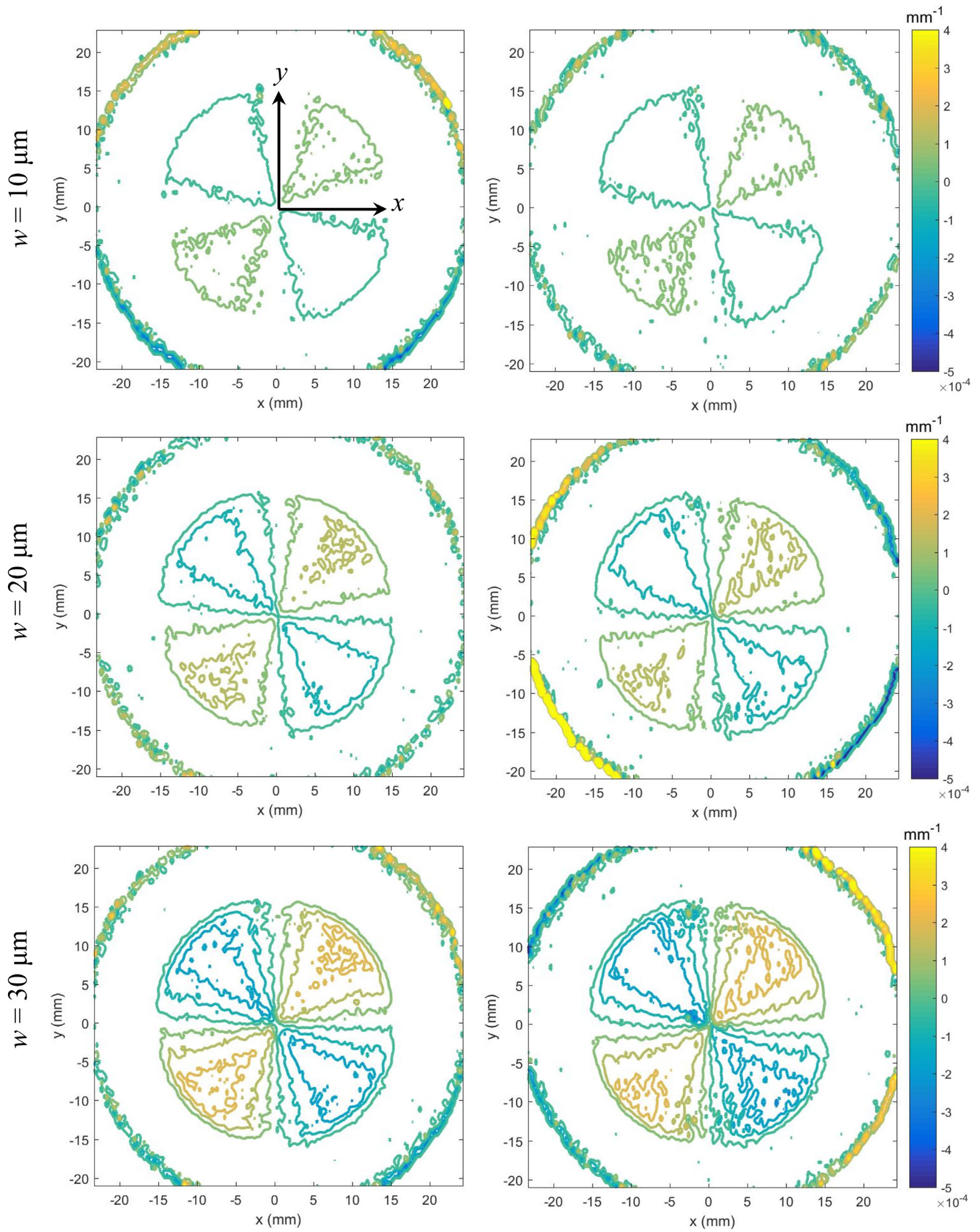

Fig. 12. Curvatures $w_{,xy}$ (left column) and $w_{,yx}$ (right column) for a clamped silicon wafer subjected to out-of-plane deformations. Note: (0, 0) is made to coincide with the center of silicon wafer. Contour increments = 7.5×10^{-5} mm^{-1}.

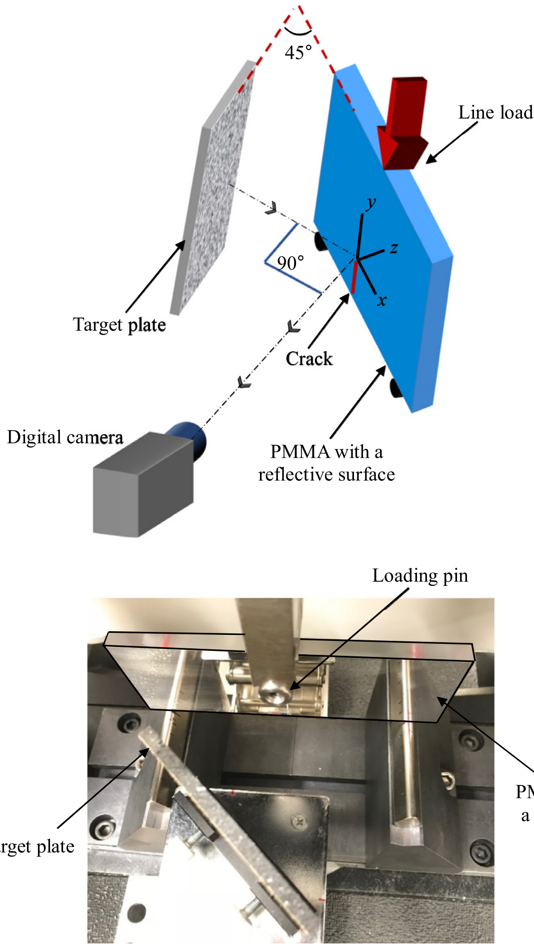

Fig. 13. Schematic of the experimental setup for quasi-static fracture study (top). Photograph of the top-view of the setup (bottom).

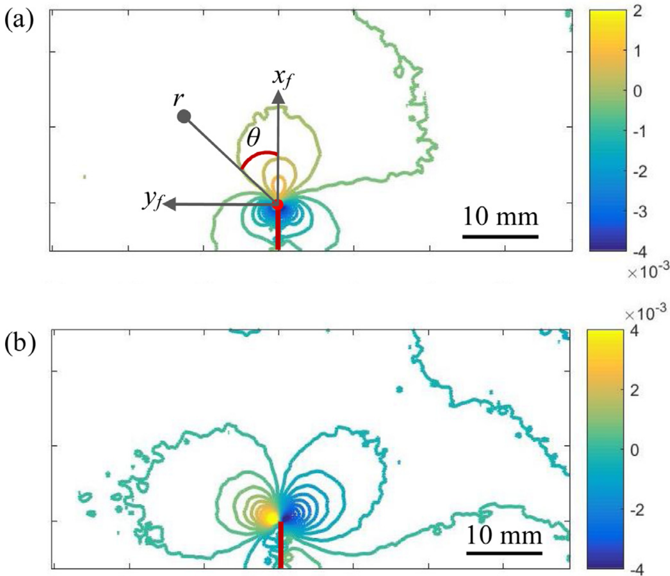

Fig. 14. Mode-I crack tip contours of surface slopes $w_{,x}$ (a) and $w_{,y}$ (b) corresponding to load of 500 N in 3-point bend PMMA specimen. Contour increments = 4×10^{-4} rad.

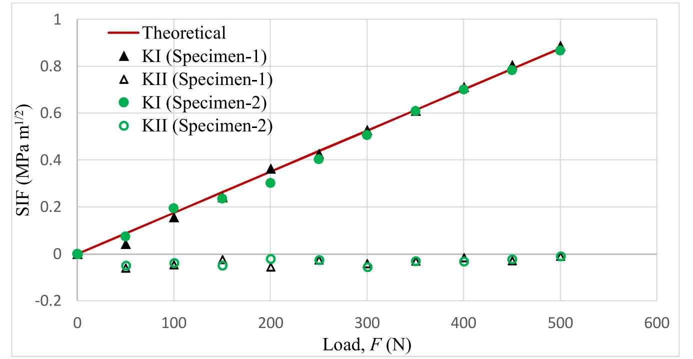

Fig. 15. Measured stress intensity factors (symbols) from simplified *r*-DGS at different load levels. The solid line represents the theoretical prediction.

as before. During image correlation, a sub-image size of 30 × 30 pixels (1 pixel = 35.18 µm) with 10 pixels overlap was used to extract the speckle displacements $\{\delta_{yo}, \delta_{xo}\}$ in the ROI. Those displacement fields were then used to compute the two orthogonal surface slopes $\{\frac{\partial w}{\partial y}, \frac{\partial w}{\partial x}\}$. It should be noted that, the experimental setup in Fig. 13 rotated about the *y*-axis, unlike the one in Fig. 5 which was rotated about the *x*-axis. Hence, appropriate attention was given when transforming $\{\frac{\partial w'}{\partial y'}, \frac{\partial w'}{\partial x'}\}$ to $\{\frac{\partial w}{\partial y}, \frac{\partial w}{\partial x}\}$.

The surface slopes of $\{\frac{\partial w}{\partial y}, \frac{\partial w}{\partial x}\}$ measured using *simplified r*-DGS at a load level of 500 N are plotted in Fig. 14. It can be observed that the contours of $\frac{\partial w}{\partial x}$ are symmetric in shape and magnitude with respect to the initial crack, the contours of $\frac{\partial w}{\partial y}$ are symmetric in shape and anti-symmetric in magnitude with respect to the initial crack. These features are similar with the traditional *r*-DGS counterparts [14,19].

The stress intensity factor (SIF) histories were evaluated using an over-deterministic least-squares analysis based on surface slopes $\frac{\partial w}{\partial x}$. The asymptotic expression for $\frac{\partial w}{\partial x}$ field around the crack-tip can be expressed as [6,19]:

$$\frac{\partial w}{\partial x} = -\frac{\upsilon t}{2E}\left\{\begin{array}{l}\sum_{N=1}^{\infty} A_N\left(\frac{N}{2}-1\right) r_f^{\left(\frac{N}{2}-2\right)} \cos\left(\frac{N}{2}-2\right)\theta_f \\ +\sum_{N=1}^{\infty} B_N\left(\frac{N}{2}-1\right) r_f^{\left(\frac{N}{2}-2\right)} \sin\left(\frac{N}{2}-2\right)\theta_f\end{array}\right\}, \quad (7)$$

where υ is the Poisson's ratio (= 0.34 for PMMA), *t* the sample thickness (= 8.6 mm), and *E* the elastic modulus (= 3.3 GPa), (r, θ) denotes the crack-tip polar coordinates as shown in Fig. 14(a). Mode-I and mode-II SIFs, K_I and K_{II}, are related to coefficients of A_1 and B_1, respectively, as $A_1 = K_I\sqrt{\frac{2}{\pi}}$ and $B_1 = K_{II}\sqrt{\frac{2}{\pi}}$. Here, the analysis utilized discrete $\frac{\partial w}{\partial x}$ data in the region around the crack-tip, $0.5 \le \frac{r}{t} \le 1.5$, $-135^\circ \le \theta \le 135^\circ$ in order to minimize the uncertainty associated with triaxial effects near the crack-tip as well as the crack-tip location. The resulting effects of non-singular far-field deformations on the measured K_I and K_{II} was offset by using four higher order terms ($N = 4$) in Eq. (7) during the least-squares analysis. The results obtained are plotted in Fig. 15 for different load levels for two different specimens. The mode-I SIFs obtained from the experiment were compared to the theoretical counterparts using [24]:

$$K_I = \frac{F\cdot S}{t\cdot W^{\frac{3}{2}}}\cdot \frac{3\left(\frac{a}{W}\right)^{\frac{1}{2}}\left[1.99-\frac{a}{W}\left(1-\frac{a}{W}\right)\left\{2.15-3.93\left(\frac{a}{W}\right)+2.7\left(\frac{a}{W}\right)^2\right\}\right]}{2\left(1+2\frac{a}{W}\right)\left(1-\frac{a}{W}\right)^{\frac{3}{2}}}, \quad (8)$$

where F is the applied load, S is the span of the beam, a is the initial crack length, t is the specimen thickness, and W is the width. The comparison is shown in Fig. 15. A good agreement between the experimental and theoretical values of SIF is evident, suggesting the feasibility of *simplified* r-DGS method to study challenging fracture mechanics problems containing sharp discontinuities and stress singularities. The mode-II SIF values are also plotted in this figure for completeness even though the loading was nominally mode-I. The resulting values of K_{II} therefore are nearly zero. The deviations here are attributed to experimental errors, which include optical and electronic noise as well as algorithmic errors in DIC, and least-squares errors.

6. Conclusions

In this work, simplification of the optical setup used for reflection-mode DGS (r-DGS) and its variants is discussed. Elimination of the beam splitter from the setup to photograph speckles on the target via the specular object surface at a known angle simplifies recording of the speckles. This hardware simplification, however, requires alterations to the governing equations in terms of coordinate transformations and linearly varying gap ('optical-arm') between the target and the object planes while interpreting the speckle shifts caused by object deformation. The necessary modifications to the governing equations have been explicitly derived and the methodology is demonstrated on two different problems. First, deformation of a clamped Si wafer subjected to central out-of-plane deflection is examined. Two orthogonal surface slopes in the whole field have been mapped and successfully compared with the elastic solution based on thin plate theory. The measurements have been post-processed by coupling the method with a higher-order least-squares-based integration algorithm to evaluate surface topography. By differentiating the slope data numerically, all three curvature components have been evaluated numerically and compared successfully with the theory. Lastly, the *simplified* r-DGSs method has been applied to crack-tip field measurement and extraction of stress intensity factors from the surface slopes using an over-deterministic least-squares analysis. The fracture parameters thus obtained closely match the theoretical predictions based on liner elastic fracture mechanics theory demonstrating the feasibility of the proposed approach to not only for optical metrology problems but as a viable experimental mechanics tool. It should be noted that the methodology described in this paper can also be used to eliminate the beam splitter in the other two DGS variants (t2-DGS and tr-DGS [19]) besides r-CGS.

Acknowledgement

Partial support for this research through Army Research Office grant W911NF-16-1-0093 is acknowledged.

References

[1] Ligtenberg FK. The moire method: a new experimental method for the determination of moments in small slab models. Proc. Soc. Exp. Stress Anal. 1954;12:83–98.
[2] Rieder G, Ritter R. Krümmungsmessung an belasteten platten nach dem ligtenbergschen moiré-verfahren. Forsch. im Ing. A 1965;33–44:31.
[3] Kao TY, Chiang FP. Family of grating techniques of slope and curvature measurements for static and dynamic flexure of plates. Opt. Eng. 1982;21(4):721–42.
[4] Chiang F-P, Juang R-M. Laser speckle interferometry for plate bending problems. Appl Opt 1976;15:2199–204.
[5] Assa A, Betser AA, Politch J. Recording slope and curvature contours of flexed plates using a grating shearing interferometer. Appled. Optics 1977;16(9):2504–13.
[6] Tippur HV, Krishnaswamy S, Rosakis AJ. Optical mapping of crack tip deformations using the methods of transmission and reflection coherent gradient sensing: a study of crack tip K-dominance. Int. J. Fract. 1991;52:91–117.
[7] Tippur HV. Simultaneous and real-time measurement of slpoe and curvature fringes in thin structures using shearing interferometry. Opt. Eng. 2004;43:3014–20.
[8] Udupa G, Ngoi BKA, Goh HCF, Yusoff MN. Defect detection in unpolished si wafers by digital shearography. Meas. Sci. Technol. 2004;15:35–43.
[9] Periasamy C, Tippur HV. Full-field digital gradient sensing method for evaluating stress gradients in transparent solids. Appl. Opt. 2012;51(12):2088–97.
[10] Periasamy C, Tippur HV. A full-field reflection-mode digital gradient sensing method for measuring orthogonal slopes and curvatures of thin structures. Meas. Sci. Technol. 2013;24:025202.
[11] Zhang R, Guo R, Cheng H. Numerical-experimental hybrid method for stress separation in digital gradient sensing method. Opt. Lasers Eng. 2015;66:122–7.
[12] Hao W, Tang C, Yuan Y, Yao X, Ma Y. Experimental study on the fiber pull-out of composites using digital gradient sensing technique. Polym. Test. 2015;41:239–44.
[13] Zhang C, Qu Z, Fang X, Feng X, Hwang K-C. Full-field measurement of surface topographies and thin film stresses at elevated temperatures by digital gradient sensing method. Appl. Opt. 2015;54:721–7.
[14] Jain AS, Tippur HV. Mapping static and dynamic crack-tip deformations using reflection-mode digital gradient sensing: applications to mode-i and mixed-mode fracture. J. Dyn. Behav. Mater. 2015;1:315–29.
[15] Jain AS, Tippur HV. Extension of reflection-mode digital gradient sensing method for visualizing and quantifying transient deformations and damage in solids. Opt. Lasers Eng. 2016;77:162–74.
[16] Miao C, Sundaram BM, Huang L, Tippur HV. Surface profile and stress field evaluation using digital gradient sensing method. Meas. Sci. Technol. 2016;27:095203.
[17] Miao C, Tippur HV. Measurement of sub-micron deformations and stresses at microsecond intervals in laterally impacted composite plates using digital gradient sensing. J. Dyn. Behav. Mater. 2018;4:336–58.
[18] Miao C, Tippur HV. Reflection-mode digital gradient sensing method: measurement accuracy. Opt. Eng. 2019;58(4):044101.
[19] Miao C, Tippur HV. Higher sensitivity digital gradient sensing configurations for quantitative visualization of stress gradients in transparent solids. Opt. Lasers Eng. 2018;108:54–67.
[20] Pan B, Qian K, Xie H, Asundi A. Two-dimensional digital image correlation for in-plane displacement and strain measurement: a review. Meas. Sci. Technol. 2009;20:062001.
[21] Pan B, Yu L, Wu D. High-Accuracy 2D digital image correlation measurements with bilateral telecentric lenses: error analysis and experimental verification. Exp. Mech. 2013;53:1719–33.
[22] Pan B. Digital image correlation for surface deformation measurement: historical developments, recent advances and future goals. Meas. Sci. Technol. 2018;29:082001.
[23] Miao C, Tippur HV. Fracture behavior of carbon fiber reinforced polymer composites: an optical study of loading rate effects. Eng. Fract. Mech. 2019;207:203–21.
[24] Janssen M, Zuidema J, Wanhill R. Fracture mechanics. 2nd ed. VSSD; 2006.